Acoustic attenuation, phase and group velocities in liquid-filled pipes III: Nonaxisymmetric propagation and circumferential modes in lossless conditions

Kyungmin Baik,[a] Jian Jiang, and Timothy G. Leighton[b]
Institute of Sound and Vibration Research, University of Southampton, Highfield, Southampton, Hampshire, SO17 1BJ, United Kingdom

(Received 5 March 2012; revised 12 December 2012; accepted 13 December 2012)

Equations for the nonaxisymmetric modes that are axially and circumferentially propagating in a liquid-filled tube with elastic walls surrounded by air/vacuum are presented using exact elasticity theory. Dispersion curves for the axially propagating modes are obtained and verified through comparison with measurements. The resulting theory is applied to the circumferential modes, and the pressures and the stresses in the liquid-filled pipe are calculated under external forced oscillation by an acoustic source. This provides the theoretical foundation for the narrow band acoustic bubble detector that was subsequently deployed at the Target Test Facility (TTF) of the Spallation Neutron Source (SNS) at Oak Ridge National Laboratory (ORNL), TN.
 [http://dx.doi.org/10.1121/1.4773863]

PACS number(s): 43.20.Mv, 43.20.Hq, 43.30.Es, 43.30.Bp [DRD] Pages: 1225–1236

I. INTRODUCTION

Since Lord Rayleigh's pioneered work on wave propagation in a semi-infinite elastic half space,[1] many acoustic waveguide theories have been developed in different geometries (plane, rectangular, circular, etc.) and for various combinations of materials (vacuum, liquid, elastic solid, etc.). In circular pipes with finite thickness, several authors have studied the propagation of elastic waves in the liquid inside the tubes. However these analyses depend on assuming that the acoustic waves in the liquid and pipe materials[2,3] are uncoupled, or by use of a thin-wall approximation.[4–6] Del Grosso[7] calculated the dispersion relation for the phase speed of propagating modes inside the tube filled with inviscid liquid using exact elasticity equations which can be applied to any frequency and thickness of the tube. His predictions were experimentally verified by Lafleur and Shields[8] in the low frequency regime for a fluid-filled elastic tube. Sinha *et al.*[9] and Plona *et al.*[10] undertook both theoretical and experimental investigations for various configurations of vacuum, liquid, and tube (e.g., vacuum inside and liquid outside, or liquid both inside and outside of the tube, etc.). In very lossy pipe materials, the phase speeds and attenuations of propagating modes in the liquid-filled tube were theoretically and experimentally obtained.[11,12] However these investigations[4–12] were only limited to the axisymmetric modes. The propagation of nonaxisymmetric modes in a hollow pipe was theoretically described by Gazis.[13] Fuller and Fahy described nonaxisymmetric modes in a thin-walled cylindrical shell filled with fluid using the thin-walled shell equation.[14] Greenspon and Singer[15] calculated the dispersion curve of nonaxisymmetric modes in a fluid that was contained within thick viscoelastic cylinder that was used as a liner inside a rigid pipe. Although commercial software packages support simulations of the dispersion relation of nonaxisymmetric modes in a fluid-filled pipe,[16,17] analytic expressions for this scenario, with an accompanying comparison with measurements, are not available.

When wave motion in the tube is not propagating along the axis but is confined to the cross-sectional plane of the tube, cross-sectional motion of the tube generates purely circumferential modes. The dispersion curves of circumferential waves for liquid-filled pipes have been discussed and calculated.[18,19] Circumferential modes can be obtained by letting the axial wave number, k_z, tend to zero in the general characteristic equation for nonaxisymmetric modes. The current requirement to characterize the circumferential modes in such pipes arose from the need to design a narrow band acoustic sensor for bubble detection for the Target Test Facility (TTF) of the Spallation Neutron Source (SNS) at Oak Ridge National Laboratory (ORNL), TN.[20] The acoustic sensor-pair for bubble detection are installed on the wall of the liquid-filled pipe, and they detect the bubble-induced pressure changes, which is closely related to the dispersion of the purely circumferential modes. The dispersion relationship represents the possible eigen modes that propagate nonaxisymmetrically for a given frequency. Therefore a summation of these modes determines the pressure on the surface of the liquid-filled pipe where the pressure transducers that are key to the bubble detector will be mounted. A change in the bubble population that is present within the liquid changes the characteristics of the dispersion, which subsequently modifies the pressure on the liquid-filled pipe. Detection of this pressure variation forms the basis of the bubble monitoring system. That system has to be narrowband because budget restrictions following the 2008 global financial crash forced dramatic reductions in the bandwidth of the transducers in the original bubble detector design.[21]

Bubble sensors are required so that the correct population of helium bubbles can be added to the ~20 tons of liquid

[a]Current address: Korea Research Institute of Standards and Science, 267 Gajeong-ro, Yuseong-gu, Daejeon, Republic of Korea, 305-340.
[b]Author to whom correspondence should be addressed: Electronic mail: tgl@soton.ac.uk

mercury that are pumped through stainless steel pipelines in the SNS.[22] The correct population will reduce erosion and extend the lifetime of the vessel that contains the mercury.[23,24] Each replacement of the vessel might cost around $12M if interruption of the facility user program is taken into account (B. Riemer, personal communication, 2012). If, as the beam power of the facility approaches its design value, replacement of the vessel were to be more frequent (as a result of cavitation erosion) than that allowed for in the business plan (when the vessel replacement schedule was based on the embrittlement of the steel as a result of radiation damage), this would incur significant costs not built into the original plan.

The present study firstly shows the correct and explicit matrix elements of nonaxisymmetric modes in a liquid-filled tube, and displays the dispersion curves in phase speed and attenuation in Sec. II. Section III discusses the circumferential modes of the liquid-filled tube and compares the predictions with those of a Finite Element simulation. In order to lay the theoretical foundation of the narrow band acoustic sensor that will be installed on the pipeline in SNS TTF at ORNL, the pressure fields in the liquid-filled tube associated with circumferential modes are investigated under a given cross-sectional forced excitation in Sec. IV.

II. AXIALLY PROPAGATING NONAXISYMMETRIC MODES

A. Displacement vector

Consider a system comprising of the elastic pipe filled with water that is shown in Fig. 1. In an elastic tube that is filled with an inviscid liquid and surrounded on the outside of the tube by vacuum, a displacement vector $\vec{u}$ can be expressed in terms of the scalar potential, ϕ, and the vector potential, $\vec{\psi}$, as $\vec{u} = \nabla\phi + \nabla \times \vec{\psi}$. The general solutions to the scalar and vector potentials which satisfy the Helmholtz equation in cylindrical coordinates are

$$\phi(r,\theta,z) = \phi_0 \varsigma_n(q_c r)\cos n\theta e^{i(k_z z-\omega t)}, \tag{1a}$$

$$\psi_r(r,\theta,z) = -C_2 \xi_{n+1}(q_s r)\sin n\theta e^{i(k_z z-\omega t)}, \tag{1b}$$

$$\psi_\theta(r,\theta,z) = C_2 \xi_{n+1}(q_s r)\cos n\theta e^{i(k_z z-\omega t)}, \tag{1c}$$

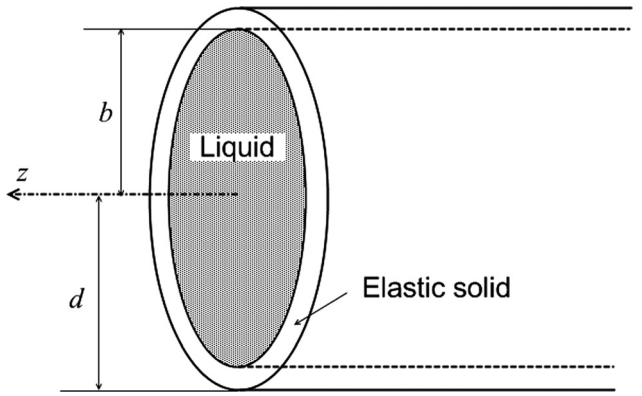

FIG. 1. Geometry of infinite liquid cylinder. The inner and outer radii are b and d, respectively.

$$\psi_z(r,\theta,z) = C_3 \xi_n(q_s r)\sin n\theta e^{i(k_z z-\omega t)}, \tag{1d}$$

where $q_c^2 = k_c^2 - k_z^2$ and $q_s^2 = k_s^2 - k_z^2$. The wave numbers, k_c and k_s are related to the circular frequency ω as $k_c = \omega/c_c$ and $k_s = \omega/c_s$, respectively, and c_c and c_s are the longitudinal and shear speeds of sound in an elastic material. The axial wave number along the axis of the cylinder is k_z.

Equations (1a)–(1d) are simplified notations of the summation of the infinite series with respect to n from $n=0$ to $n=\infty$ terms. The coefficients ϕ_0, C_2, and C_3 are unknowns associated with ς_n and ξ_n representing the Bessel functions of the order n which are associated with q_c (longitudinal) and q_s (shear), respectively. Since the term $\exp[i(k_z z - \omega t)]$ is common in every equation above, this is omitted for simplicity, but this term is important in the calculation of the displacement and stress tensors. The displacement vectors in an *inviscid* liquid (subscripted as l) and in an elastic solid (subscripted as e) are expressed as follows:

$$\vec{u}_l = \hat{r}\left[-q_l A J_{n+1}(q_l r) + \frac{n}{r} A J_n(q_l r)\right]\cos n\theta + \hat{\theta}\left[-\frac{n}{r} A J_n(q_l r)\right]\sin n\theta + \hat{z}[ik_z A J_n(q_l r)]\cos n\theta, \tag{2a}$$

$$\begin{aligned}\vec{u}_e = {} & \hat{r}\Big\{-q_c[CJ_{n+1}(q_c r) + DY_{n+1}(q_c r)] + \frac{n}{r}[CJ_n(q_c r) + DY_n(q_c r)] - ik_z[EJ_{n+1}(q_s r) + FY_{n+1}(q_s r)] \\ & + \frac{n}{r}[GJ_n(q_s r) + HY_n(q_s r)]\Big\}\cos n\theta + \hat{\theta}\Big\{-\frac{n}{r}[CJ_n(q_c r) + DY_n(q_c r)] - ik_z[EJ_{n+1}(q_s r) + FY_{n+1}(q_s r)] \\ & + q_z[GJ_{n+1}(q_s r) + HY_{n+1}(q_s r)] - \frac{n}{r}[GJ_n(q_s r) + HY_n(q_s r)]\Big\}\sin n\theta + \hat{z}\{ik_z[CJ_n(q_c r) + DY_n(q_c r)] \\ & + q_s[EJ_n(q_s r) + FY_n(q_s r)]\}\cos n\theta,\end{aligned} \tag{2b}$$

where $q_l^2 = k_1^2 - k_z^2$, $k_1 = \omega/c_1$, c_1 is the intrinsic sound speed in liquid, and J and Y represent Bessel functions of first and second kinds, respectively. During the derivation, the relationships $\zeta'_n(x) = -\varsigma_{n+1}(x) + (n/x)\varsigma_n(x)$ and $\xi'_{n+1}(x) = \xi_n(x) - (n+1)/x\xi_{n+1}(x)$ are used.[25] The above result is reduced to the displacement vectors for the axisymmetric modes when $n=0$ is substituted. The unknown coefficients, A, C, D, E, F, G, and H are found from the

boundary conditions. In the liquid, only Bessel functions of first kind are considered since Y_n diverges at the center ($r = 0$) of the tube.

B. Stress tensor

The stress tensor elements of τ_{rr}, $\tau_{r\theta}$, and τ_{rz} in cylindrical coordinates can be obtained from following equations:

$$\tau_{rr} = \lambda\left(\frac{\partial u_r}{\partial r} + \frac{u_r}{r} + \frac{1}{r}\frac{\partial u_\theta}{\partial \theta} + \frac{\partial u_z}{\partial z}\right) + 2\mu\frac{\partial u_r}{\partial r}, \tag{3a}$$

$$\tau_{r\theta} = \mu\left(\frac{1}{r}\frac{\partial u_r}{\partial \theta} + \frac{\partial u_\theta}{\partial r} - \frac{u_\theta}{r}\right), \tag{3b}$$

$$\tau_{rz} = \mu\left(\frac{\partial u_r}{\partial z} + \frac{\partial u_z}{\partial r}\right), \tag{3c}$$

where λ and μ are Lamé constants. Substituting elements of the displacement vector into the above equation, the stress tensor elements in liquid and in an elastic solid are as follows:

$$\tau_{rrl} = -\rho_1\omega^2 A J_n(q_l r)\cos n\theta, \tag{4a}$$

$$\tau_{r\theta l} = \tau_{rzl} = 0, \tag{4b}$$

$$\begin{aligned}\tau_{rre} = \Big\{ & -\lambda_e(q_c^2 + k_z^2)[CJ_n(q_c r) + DY_n(q_c r)] \\ & + 2\mu_e\left[\frac{q_c}{r}\{CJ_{n+1}(q_c r) + DY_{n+1}(q_c r)\} + \left(-q_c^2 + \frac{n(n-1)}{r^2}\right)\{CJ_n(q_c r) + DY_n(q_c r)\}\right] \\ & + 2\mu_e\left[\frac{(n+1)ik_z}{r}\{EJ_{n+1}(q_s r) + FY_{n+1}(q_s r)\} - ik_z q_s\{EJ_n(q_s r) + FY_n(q_s r)\}\right] \\ & + 2\mu_e\left[-\frac{nq_s}{r}\{GJ_{n+1}(q_s r) + HY_{n+1}(q_s r)\} + \frac{n(n-1)}{r^2}\{GJ_n(q_s r) + HY_n(q_s r)\}\right]\Big\}\cos n\theta,\end{aligned} \tag{4c}$$

$$\begin{aligned}\tau_{r\theta e} = \mu_e\Big[& \frac{2nq_c}{r}\{CJ_{n+1}(q_c r) + DY_{n+1}(q_c r)\} - \frac{2n(n-1)}{r^2}\{CJ_n(q_c r) + DY_n(q_c r)\} \\ & + \frac{2(n+1)ik_z}{r}\{EJ_{n+1}(q_s r) + FY_{n+1}(q_s r)\} - ik_z q_s\{EJ_n(q_s r) + FY_n(q_s r)\} \\ & - \frac{2q_s}{r}\{GJ_{n+1}(q_s r) + HY_{n+1}(q_s r)\} + \left(q_s^2 - \frac{2n(n-1)}{r^2}\right)\{GJ_n(q_s r) + HY_n(q_s r)\}\Big]\sin n\theta,\end{aligned} \tag{4d}$$

$$\begin{aligned}\tau_{rze} = \mu_e\Big[& -2ik_z q_c\{CJ_{n+1}(q_c r) + DY_{n+1}(q_c r)\} + \frac{2nik_z}{r}\{CJ_n(q_c r) + DY_n(q_c r)\} + (k_z^2 - q_s^2)\{EJ_{n+1}(q_s r) + FY_{n+1}(q_s r)\} \\ & + \frac{nq_s}{r}\{EJ_n(q_s r) + FY_n(q_s r)\} + \frac{nik_z}{r}\{GJ_n(q_s r) + HY_n(q_s r)\}\Big]\cos n\theta,\end{aligned} \tag{4e}$$

where ρ_1 is density of liquid. In an inviscid liquid, the shear stresses in the liquid vanish as shown in Eq. (4). In the solid, the shear stress of $\tau_{r\theta e}$ becomes zero in the axisymmetric mode ($n = 0$). Moreover, in the axisymmetric case, the problem is further simplified since all the terms associated with the coefficients G and H in the normal stresses τ_{rre} and τ_{rze} vanish.

C. Boundary conditions and nontrivial solutions

Neglecting the viscosity of the liquid, the boundary conditions imposed on the structure in Fig. 1 are the continuity of normal displacements, the continuity of normal stresses, and the vanishing of the shear stresses at $r = b$ and d, respectively. The number of unknown coefficients is seven. However, instead of applying the continuity of normal displacements and stresses separately, from the continuity of the ratio of normal displacements to normal stresses, the unknown coefficient A can be eliminated. Thus, six boundary conditions are imposed as follows, which generates six independent equations associated with six unknowns (C–H).

$$\begin{aligned}&\left.\frac{\tau_{rrl}}{\vec{u}_l\cdot\hat{r}}\right|_{r=b} = \left.\frac{\tau_{rre}}{\vec{u}_e\cdot\hat{r}}\right|_{r=b}, \quad \left.\frac{\tau_{rre}}{\vec{u}_e\cdot\hat{r}}\right|_{r=d} = 0, \\ &\tau_{r\theta e}|_{r=b} = \tau_{rze}|_{r=b} = 0, \quad \tau_{r\theta e}|_{r=d} = \tau_{rze}|_{r=d} = 0.\end{aligned} \tag{5}$$

From Eqs. (2)–(5), six independent equations are obtained. The condition for obtaining nontrivial solutions to six unknown coefficients generates the following characteristic equation:

$$|d_{ij}| = 0, \quad (i, j = 1\text{–}6), \tag{6}$$

which states that the determinant of the 6×6 matrix with the element of d_{ij} should vanish. Each matrix element d_{ij} is calculated as follows:

$$
\begin{aligned}
d_{11} &= \frac{nq_c}{b} J_{n+1}(q_c b) - \frac{n(n-1)}{b^2} J_n(q_c b), \\
d_{12} &= \frac{nq_c}{b} Y_{n+1}(q_c b) - \frac{n(n-1)}{b^2} Y_n(q_c b), \\
d_{13} &= \frac{(n+1)ik_z}{b} J_{n+1}(q_s b) - \frac{ik_z q_s}{2} J_n(q_s b), \\
d_{14} &= \frac{(n+1)ik_z}{b} Y_{n+1}(q_s b) - \frac{ik_z q_s}{2} Y_n(q_s b), \\
d_{15} &= -\frac{q_s}{b} J_{n+1}(q_s b) + \left\{ \frac{q_s^2}{2} - \frac{n(n-1)}{b^2} \right\} J_n(q_s b), \\
d_{16} &= -\frac{q_s}{b} Y_{n+1}(q_s b) + \left\{ \frac{q_s^2}{2} - \frac{n(n-1)}{b^2} \right\} Y_n(q_s b),
\end{aligned} \tag{7a}
$$

$$
d_{21} - d_{26} = d_{11} - d_{16}|_{b \to d}, \tag{7b}
$$

$$
\begin{aligned}
d_{31} &= ik_z q_c J_{n+1}(q_c b) - \frac{nik_z}{b} J_n(q_c b), \\
d_{32} &= ik_z q_c Y_{n+1}(q_c b) - \frac{nik_z}{b} Y_n(q_c b), \\
d_{33} &= -PJ_{n+1}(q_s b) - \frac{nq_s}{2b} J_n(q_s b), \\
d_{34} &= -PY_{n+1}(q_s b) - \frac{nq_s}{2b} Y_n(k_s b), \\
d_{35} &= -\frac{nik_z}{2b} J_n(q_s b), \quad d_{36} = -\frac{nik_z}{2b} Y_n(q_s b),
\end{aligned} \tag{7c}
$$

$$
d_{41} - d_{46} = d_{31} - d_{36}|_{b \to d}, \tag{7d}
$$

$$
\begin{aligned}
d_{51} &= q_c \frac{1 + bQ_n}{b} J_{n+1}(q_c b) \\
&\quad + \left\{ P + \frac{n(n - 1 - bQ_n)}{b^2} \right\} J_n(q_c b), \\
d_{52} &= q_c \frac{1 + bQ_n}{b} Y_{n+1}(q_c b) \\
&\quad + \left\{ P + \frac{n(n - 1 - bQ_n)}{b^2} \right\} Y_n(q_c b), \\
d_{53} &= ik_z \frac{n + 1 + bQ_n}{b} J_{n+1}(q_s b) - ik_z q_s J_n(q_s b), \\
d_{54} &= ik_z \frac{n + 1 + bQ_n}{b} Y_{n+1}(q_s b) - ik_z q_s Y_n(q_s b), \\
d_{55} &= -\frac{nq_s}{b} J_{n+1}(q_s b) + \frac{n(n - 1 - bQ_n)}{b^2} J_n(q_s b), \\
d_{56} &= -\frac{nq_s}{b} Y_{n+1}(q_s b) + \frac{n(n - 1 - bQ_n)}{b^2} Y_n(q_s b),
\end{aligned} \tag{7e}
$$

$$
d_{61} - d_{66} = d_{51} - d_{56}|_{b \to d,\, Q_n \to 0}, \tag{7f}
$$

where $P = k_z^2 - k_s^2/2$ and

$$
Q_n = \frac{\rho_1 \omega^2}{2\rho_e c_s^2} \frac{J_n(q_l b)}{q_l J_{n+1}(q_l b) - \frac{n}{b} J_n(q_l b)}. \tag{7g}
$$

In obtaining the expression for d_{ij}, the relationships $\lambda_e + 2\mu_e = \rho_e c_c^2$ and $\mu_e = \rho_e c_s^2$ are used (where ρ_e is the density of the elastic solid). Each matrix element in the second row ($d_{21}-d_{26}$) is obtained by replacing b with d in each element in the first row, and this is indeed the meaning of Eq. (7b). Likewise, each matrix element in the fourth row is obtained by replacing b with d in each element in the third row. Elements from the first row to the fourth row are purely related to the material properties of the elastic solid. The properties of the liquid are contained within the elements in the fifth row, wherein is found Q_n, a parameter that is similar to the acoustic impedance (while acoustic impedance is the ratio of the acoustic pressure to the velocity, Q_n is the ratio of the acoustic pressure to the displacement). Since the tube wall at $r = b$ is in contact with the liquid, Q_n takes a role in loading the acoustic properties of the liquid to the tube wall. If the volume contained in the pipe were to be vacuum, Q_n becomes 0 since $\rho_1 \to 0$. Therefore, each element in the sixth row is obtained by replacing b with d in each element in the fifth row and taking $Q_n \to 0$ to reflect the fact that, in the SNS TTF scenario considered here, the material outside of the tube (air) is approximated to be a vacuum.

Equations (7a) and (7b) are the terms associated with $\sin n\theta$. Hence, in the limit of $n = 0$ (the axisymmetric case), only four equations from Eqs. (7c) to (7f) are taken into consideration and all the terms associated with G and H (5th and 6th columns) vanish. This is the case that corresponds to Eqs. (4a)–(4d) in Ref. 8.

D. Dispersion curves

When the frequency and the mode index (n) are given, the axial wave number (k_z) is found to satisfy Eq. (6). Theoretically, throughout the entire frequency domain, there exists an infinite number of axial wave numbers that satisfy Eq. (6). However, for a given frequency, only a certain number of axial wave numbers are permitted, since each mode has a cut-off frequency that is the lowest frequency that a mode will propagate in the tube system. Among the solutions to k_z, the largest value of k_z is associated with the lowest mode, since the phase speed of the mode is inversely proportional to the wave number, k_z. Therefore, in this study, the mode is identified by two indices n and m such as (n, m) mode where n, $m \geq 0$. Axisymmetric modes are represented by (0, m) modes.

Figure 2 shows dispersion curves of phase (solid) and group (dashed) speeds for several modes in a water-filled PMMA tube which has 4.445 cm inner radius and 0.5 cm wall thickness (for details see Refs. 11, 12, and 26). The longitudinal and shear sound speeds of PMMA are 2.690 km s^{-1} and 1.340 km s^{-1}, respectively. The sound speed in water used in this calculation is 1.479 km s^{-1}. The densities of water and PMMA are 1000 kg m^{-3} and 1190 kg m^{-3}, respectively. Since PMMA is an acoustically very lossy material, the longitudinal and shear absorptions of PMMA were included in our calculations. For the acoustic properties and details of the material damping of the PMMA, see Ref. 27. The dimensionless coordinate used along the horizontal axis in the graphs ($k_1 b$) is the product of the wavenumber in the liquid and the inner radius. The vertical axis in the graphs shows the phase speed (c_p) and

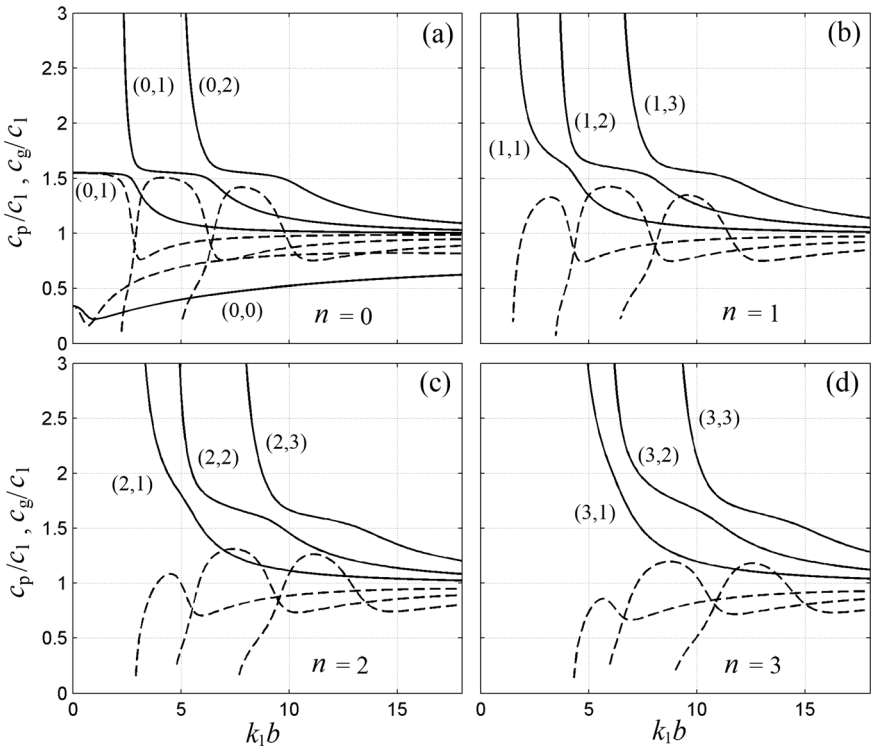

FIG. 2. Dispersion curves of phase speed (solid) and group speed (dashed) of modes for water-filled PMMA tube. (a) The first few axisymmetric modes and (b)–(d) some nonaxisymmetric modes.

group speed (c_g) normalized by the speed of sound in liquid (c_1). The axisymmetric modes in Fig. 2(a) were obtained when $n = 0$. The nonaxisymmetric modes are displayed in Figs. 2(b)–2(d). While the two lowest axisymmetric modes exist at the zero-frequency limit, all the nonaxisymmetric modes exhibit cut-off frequencies, meaning that such a mode only propagates above its cut-off frequency. While phase speeds diverge at their cut-off frequencies, the group speeds converge to 0.

Figure 3 shows the theoretical prediction for the attenuation of each mode (in dB m^{-1}), plotted against the dimensionless product of the wavenumber in the liquid and the inner radius for the same water-filled PMMA tube as was used for Fig. 2. The attenuation was calculated by replacing the real longitudinal and shear wave numbers in the elastic solids, k_c, k_s, and real wave number in the liquid, k_1, with complex wave numbers k_c', k_s', and k_1', respectively. This is done by including the material absorption of the elastic solid in k_c and

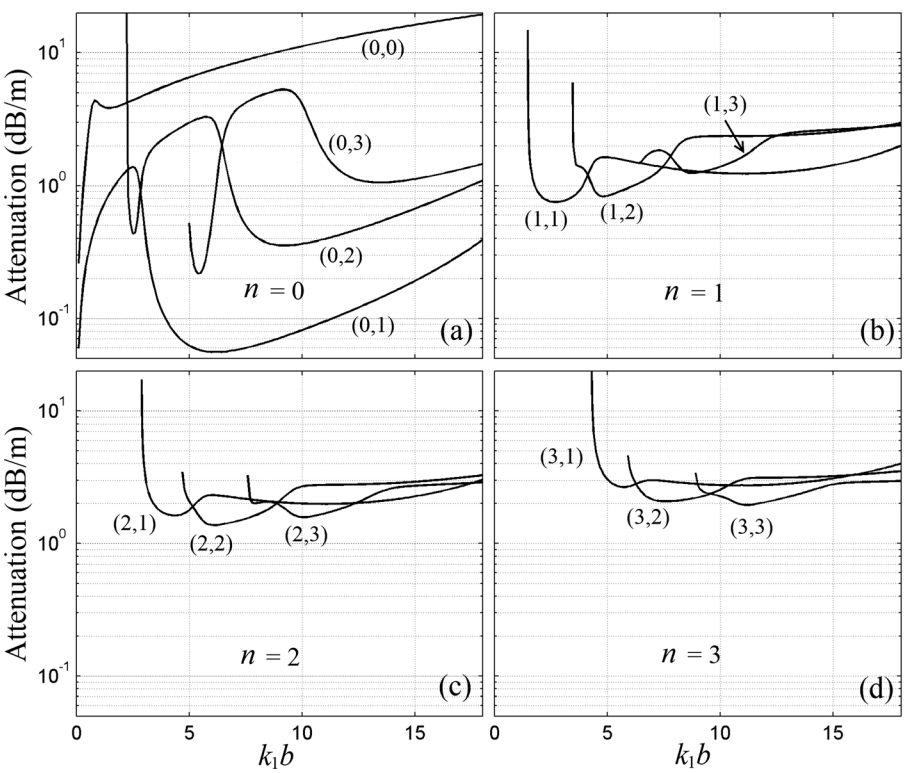

FIG. 3. Dispersion curves of attenuation of modes for water-filled PMMA tube. (a) The first few axisymmetric modes and (b)–(d) some nonaxisymmetric modes.

k_s, and including viscosities and thermal conductivities of the liquid in k_1, as is explained in Ref. 11. When the complex wave numbers, k_c', k_s', and k_1' are substituted into the matrix elements in Eq. (7), the solution to k_z is found in the complex space, and its real and imaginary parts determine the phase speed and the attenuation, respectively.

Nonaxisymmetric modes can be experimentally observed in the $k-\omega$ space that is obtained using a two-dimensional (spatially and temporally) Fourier transform of hydrophone measurements taken along the axis of the tube as explained in Ref. 11. Figure 4(a) shows the measured $k-\omega$ map in the water-filled PMMA tube, using the experimental method described in Ref. 11. The color scheme represents the signal amplitude in a dB scale. The bright features represent the dominant modes existing in the water-filled PMMA tube: three axisymmetric modes and three nonaxisymmetric modes are labeled in Fig. 4(a). For clarity, the theoretical predictions of Eq. (6) are not overlaid on these experimental data but instead are plotted below them in Fig. 4(b). The open circles in Fig. 4(b) are measurements which represent the locations of the bright features in Fig. 4(a) and show good agreement with the theoretical predictions (solid curves). For reasons explained in Ref. 11, each measured mode is only visible over particular frequency bands in Fig. 4(a), even though the predictions of Eq. (6) suggest continuous curves in Fig. 4(b). Furthermore some predicted modes in Fig. 3(b) are not observable at all in the measured data in Fig. 4(a). Other modes such as (2, m) and (3, m) etc. are not observed in this measurement. Comparing Fig. 4(a) to Fig. 4(b), nonaxisymmetric modes as well as axisymmetric modes are clearly observed and the theoretical calculations correspond very well to the measurements, which validates the theory presented in this study.

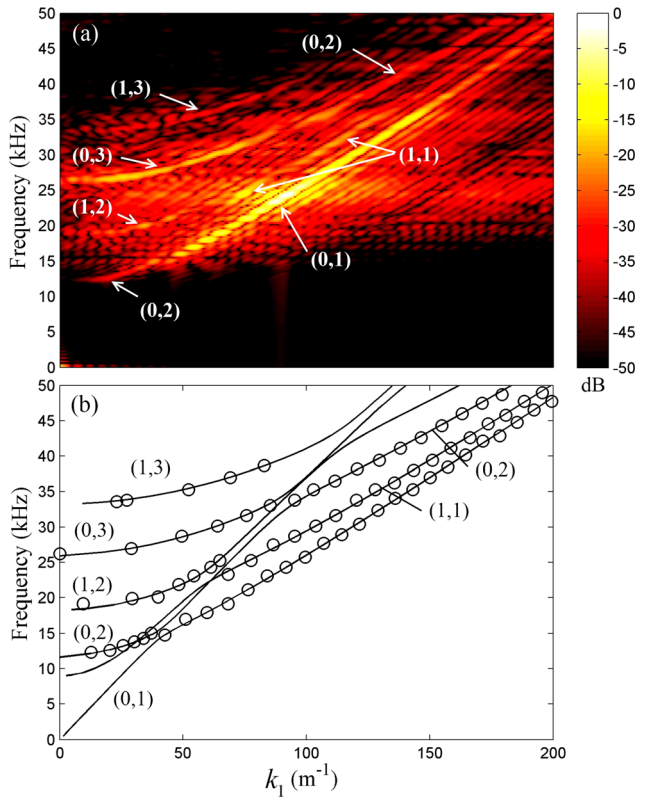

FIG. 4. (Color online) (a) Two-dimensional spectrum of the measured signal array along the axis of the water-filled PMMA tube (Ref. 11) and (b) theoretical loci of the axisymmetric and nonaxisymmetric modes that are observed in (a).

III. CIRCUMFERENTIALLY PROPAGATING MODES

A. Characteristic equation

Circumferential modes can be obtained from Eqs. (6) and (7) by substituting into them $k_z \to 0$. This causes the motion of the particles in the liquid and the solid to be purely cross-sectional. In this limit, the matrix elements in Eqs. (7a)–(7f) are simplified. Moreover, following matrix elements become zero:

$$d_{13} = d_{14} = d_{23} = d_{24} = d_{53} = d_{54} = d_{63} = d_{64}|_{k_z \to 0} = 0,$$
$$d_{31} = d_{32} = d_{35} = d_{36} = d_{41} = d_{42} = d_{45} = d_{46}|_{k_z \to 0} = 0. \tag{8}$$

This causes the determinant of the matrix to be the product of the determinants of 4×4 and 2×2 matrices. The elements of the 4×4 matrix are provided by all the nonzero elements in the 1st, 2nd, 5th, and 6th rows. The elements of the 2×2 matrix are provided by all the nonzero elements in 3rd and 4th rows. Consequently, the characteristic equation [Eq. (6)] for the circumferential modes is expressed as

$$\begin{vmatrix} d_{11}' & d_{12}' & d_{15}' & d_{16}' \\ d_{21}' & d_{22}' & d_{25}' & d_{26}' \\ d_{31}' & d_{32}' & d_{55}' & d_{56}' \\ d_{41}' & d_{42}' & d_{65}' & d_{66}' \end{vmatrix} \begin{vmatrix} d_{33}' & d_{34}' \\ d_{43}' & d_{44}' \end{vmatrix} = 0, \tag{9}$$

where all the primed notation denotes the value of the matrix element in the limit of $k_z \to 0$. Equation (9) shows that there exist two kinds of circumferential waves. One is the wave satisfying the condition when the first determinant is zero (plane-strain vibration), and the other is the wave satisfying the condition when the second determinant is zero (longitudinal-shear vibration).[13] In particular, the second determinant in Eq. (9) is briefly expanded as follows:

$$bdk_s^2 L_{n+1,n+1}(k_s) - ndk_s L_{n+1,n}(k_s) - nbk_s L_{n,n+1}(k_s) + n^2 L_{n,n}(k_s) = 0, \tag{10}$$

where $L_{mn}(y)$ is the Wronskian defined by $L_{mn}(y) = J_m(dy)Y_n(by) - J_n(by)Y_m(dy)$. Equation (10) is solely dependent on the shear wave number, k_s, and this means that the longitudinal speed in the tube material does not contribute to this kind of vibration. Equation (10) is not applied to the axisymmetric mode ($n = 0$) since the characteristic equation for the axisymmetric modes cannot be resolved in this way. When the first determinant is 0, the resulting characteristic equation is dependent on both the longitudinal and shear speeds of the tube material.

The phase speed of the circumferential wave at $n = 0$ is infinite since it is inversely proportional to the mode index, n. At a given frequency, ω, the phase speed of the circumferential wave (creeping wave), c_f, normalized by the intrinsic speed of sound in liquid, c_1, is found from the relation of

$c_f/c_1 = k_1 d/n$ (where d is outer radius of the tube), where n satisfies Eq. (9).[19] Consequently, the number, n, need not necessarily be an integer, but it does need to be real when there is no absorption (to account for finite absorption, this number can be extended to the complex space). In particular, when n becomes integer, the system resonates and the corresponding frequency becomes a resonance frequency. The resonance condition is imposed when the circumference of the tube is the same as a multiple of the wavelength of the creeping wave.

B. Dispersion relation

Figure 5 uses Eq. (9) to calculate the phase velocity of circumferential waves on a water-filled PMMA cylinder which has the same dimension as that used in the calculation of Fig. 2. Figure 5 plots the phase speed (normalized by the speed of sound in water) as a function of the product of the wavenumber in water and the outer radius. There exist infinite numbers of circumferential modes. Plane-strain modes are denoted by PSm where m is modal index, and the longitudinal-shear mode is denoted by LS.[13] While an infinite number of PS loci exist, there is only one LS loci obtained from Eq. (9). PS curves are obtained from the first determinant of Eq. (9). The LS mode which is explicitly shown in Eq. (10) gives only one solution, which is almost constant throughout the frequency. The phase speed of the PS1 mode becomes 0 at the zero frequency limit and increases with increasing frequency. Other modes (PS2 and higher) diverge as frequency decreases and their phase speed become infinite at their cut-off frequencies.

C. Resonance frequency and the shape of the modes

The resonance frequencies of the modes can be obtained using two methods. One approach is to find, from Fig. 5, the frequencies where the circumference of the tube equals an integer number of multiples of the wavelength of the mode (the principle of phase matching).[19] This method can be readily applied to a cylinder or a thick shell. Since the wavelength of the circumferential wave is approximately given by $2\pi d/n$ for a thin-walled pipe, n should be an integer to satisfy the condition that the circumference of the tube is an integer number of multiples of the wavelength. Consequently, the resonance frequency can be found by searching the intersection of the curves in Fig. 5 with the following function by varying the index, n, as 1, 2, 3,…

$$\frac{c_f}{c_1} = \frac{kd}{n}. \tag{11}$$

The other method of finding the resonance frequencies is by using Eq. (9) directly. Substituting $n = 0, 1, 2, \ldots$ into either the first or the second determinant, the frequency which satisfies Eq. (9) is a resonance frequency.

The integer index n is related to the shape of the motion where creeping waves that exhibit such displacement display resonance frequencies. In such a condition, the circumference of the tube becomes equal to an integer multiple of the wavelength when the index n is an integer. Each value of $n = 0$ through 3 corresponds to the cross-sectional motion of the tube as shown in Fig. 6, which was obtained through simulation of the eigen modes of the water-filled PMMA tube. This simulation was made by the Finite Element Method through the commercial software of COMSOL. The deformation of the structure is exaggerated to show the mode shape of the tube. The bright to dark grey scheme represents the positive to negative magnitude of the normal stress in the liquid (which is the acoustic pressure multiplied by -1) and the tube material. The breathing mode ($n = 0$), translational mode ($n = 1$), dipole mode ($n = 2$), and tripole mode ($n = 3$) are illustrated in Figs. 6(a)–6(d), respectively. As the mode

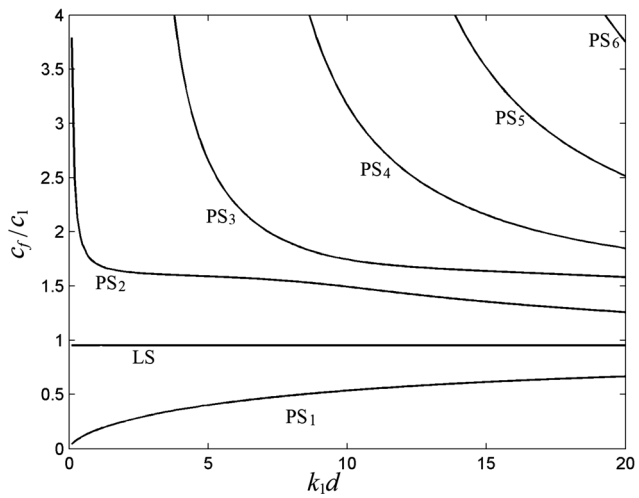

FIG. 5. Phase speed of the circumferential waves on water-filled PMMA cylinder.

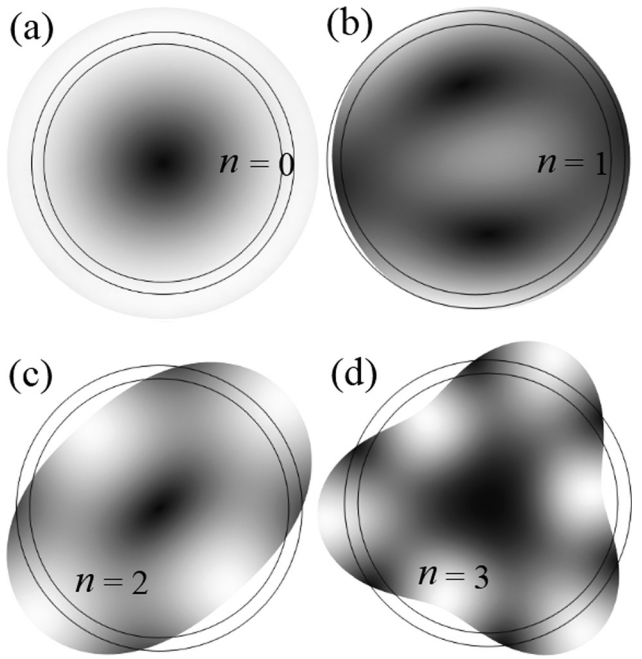

FIG. 6. Finite Element simulation for the cross-sectional mode of the water-filled PMMA tube surrounded by vacuum at each resonance frequency. The resting positions of the inner and outer tube walls are shown by the two concentric circles on each panel. The bright to dark color scheme represents the positive to negative magnitude of the acoustic pressure in the liquid (which is the normal stress multiplied by -1) and the normal stress in the tube. Wall displacement was exaggerated to show the mode shape clearly.

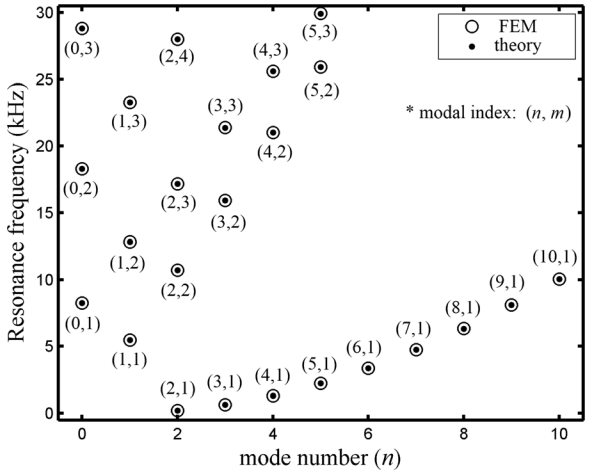

FIG. 7. Comparison of the resonance frequencies of water-filled PMMA tube found from the theory (filled circles) and the FEM simulation (open circles). At each mode, resonance frequencies predicted by the theory developed in the current study exactly correspond to the FEM calculations.

number, n, increases, the number of nodes and the antinodes also increases.

Figure 7 plots the resonance frequencies of some modes against the mode indices, n, comparing several resonance frequencies for the water-filled PMMA tube predicted by the theory (filled circles) and by the Finite Element simulation (open circles) which used a 2D frequency domain Acoustic-Solid interaction module provided by COMSOL with quad mesh having a maximum element size of 2.8 mm. The COMSOL's *Eigen-frequency* solver was used to determine the resonance frequencies. The dimension of the tube system is the same as that at the ORNL, which is, 6.4097 cm inner radius and 0.6553 cm wall thickness. Each mode is denoted by modal index (n, m). The Finite Element simulation (FEM) shows an excellent agreement with the calculations predicted by the theory proposed in the current study.

IV. FORCED OSCILLATION

A. External excitation and boundary condition

When an external excitation is applied to the fluid-filled tube, its response changes as a function of frequency. Such excitation may be axial or cross-sectional. In this study, only the cross-sectional excitation (which is independent of axial coordinates) is assumed to exist. Consequently the applied pressure P_1 is expressed as $P_1 = P_1(\theta)\exp(-i\omega t)$ where θ is azimuthal angle. When the source excites the tube symmetrically with respect to $\theta = 0$ as shown in Fig. 8(a), the applied pressure is expanded by Fourier series as follows:

$$P_1 = \sum_{n=0}^{\infty} p_{1n}\cos n\theta, \quad p_{1n} = \frac{\varepsilon_n}{\pi}\int_{-\pi}^{\pi} P_1(\theta')\cos n\theta' d\theta', \tag{12}$$

where ε_n is 1 at $n = 0$, and $\varepsilon_n = 2$ for all other values of n. In this situation, the boundary condition changes at $r = d$ owing to the presence of the external pressures. Thus, from Eqs. (4c) and (12), the continuity of the normal stress at $r = d$ (when $k_z \to 0$) gives

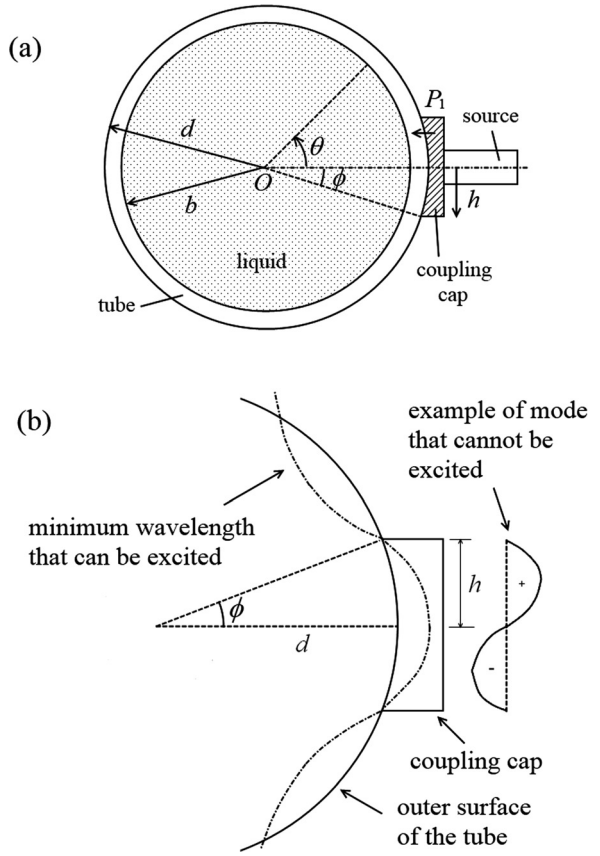

FIG. 8. (a) Configuration of the forced excitation of the tube and (b) geometry of the actual coupling cap used by TTF SNS to excite the outer surface of the tube. The area in contact with the coupling cap is characterized by the angle ϕ. Inside this area of contact, the partial wave cannot change its phase if the source is piston-like.

$$\begin{aligned}
&\left[\frac{k_c}{d}J_{n+1}(k_c d) + \left\{-\frac{k_s^2}{2} + \frac{n(n-1)}{d^2}\right\}J_n(k_c d)\right]C \\
&+\left[\frac{k_c}{d}Y_{n+1}(k_c d) + \left\{-\frac{k_s^2}{2} + \frac{n(n-1)}{d^2}\right\}Y_n(k_c d)\right]D \\
&+\left[-\frac{nk_s}{d}J_{n+1}(k_s d) + \frac{n(n-1)}{d^2}J_n(k_s d)\right]G \\
&+\left[-\frac{nk_s}{d}Y_{n+1}(k_s d) + \frac{n(n-1)}{d^2}Y_n(k_s d)\right]H = \frac{p_{1n}}{2\mu_e}.
\end{aligned} \tag{13}$$

The right-hand side of the equation represents the forcing term. Therefore, the equation of the cross-sectional motion of the system (when $k_z \to 0$) imposed by the forced oscillation on the outer surface of the tube is described as

$$\begin{bmatrix} d'_{11} & d'_{12} & 0 & 0 & d'_{15} & d'_{16} \\ d'_{21} & d'_{22} & 0 & 0 & d'_{25} & d'_{26} \\ 0 & 0 & d'_{33} & d'_{34} & 0 & 0 \\ 0 & 0 & d'_{43} & d'_{44} & 0 & 0 \\ d'_{51} & d'_{52} & 0 & 0 & d'_{55} & d'_{56} \\ d'_{61} & d'_{62} & 0 & 0 & d'_{65} & d'_{66} \end{bmatrix} \begin{bmatrix} C \\ D \\ E \\ F \\ G \\ H \end{bmatrix} = \begin{bmatrix} 0 \\ 0 \\ 0 \\ 0 \\ 0 \\ p_{1n}/(2\mu_e) \end{bmatrix}. \tag{14}$$

Equation (14) determines the value of coefficients, C, D, E, F, G, and H explicitly. In the calculation of the coefficients, the elements, d'_{33}, d'_{34}, d'_{43}, d'_{44} do not affect the calculation. This is because the determinant composed of such elements is a common factor in this calculation of the coefficients. This in turn is a consequence of the property that the determinant of the 6×6 matrix can be resolved as the product of determinants of two matrices as shown in Eq. (9). When those coefficients are substituted into Eqs. (2) and (4) (when $k_z \to 0$), the displacements and stress elements in the liquid and the elastic solid can be calculated. As is evident in Eq. (14), the value of the coefficients E and F are 0. The value of the coefficient A can be obtained from either continuity of the normal displacement or the normal stress at the inner wall of the tube ($r = b$).

B. Point source and actual source

In the geometry in Fig. 8, the Fourier coefficient p_{1n} is defined by the kind of source and therefore may take various forms. As a first example, suppose that there is an ideal point source at $\theta = 0$, which can be configured as $P_1(\theta') = P_{10}^{\text{point}}\delta(\theta)$. In cylindrical coordinates, the delta function with respect to the azimuthal angle is defined as

$$\delta(\theta) = \frac{1}{2\pi}\sum_{n=-\infty}^{\infty} e^{in\theta} = \frac{1}{2\pi} + \frac{1}{2\pi}\sum_{n=1}^{\infty}(e^{in\theta} + e^{-in\theta}) = \frac{1}{2\pi}\sum_{n=0}^{\infty}\varepsilon_n \cos n\theta. \tag{15}$$

The delta function is therefore automatically decomposed by the terms with mode index, n, thus, relating Eq. (15) with Eq. (12),

$$P_1 = P_{10}^{\text{point}}\delta(\theta) = \sum\frac{P_{10}^{\text{point}}}{2\pi}\varepsilon_n \cos n\theta = \sum p_{1n}\cos n\theta, \tag{16}$$

and coefficient, p_{1n} is calculated as

$$p_{1n} = \frac{P_{10}^{\text{point}}\varepsilon_n}{2\pi}. \tag{17}$$

However, in the practical instrument for SNS TTF that this paper underpins, the source is not so simple. A coupling cap (flat on one side, and curved to match the outer wall of the pipe on the other; Fig. 8) is placed between the flat faceplate of the transducer and the outer wall of the pipe (otherwise the curvature of the pipe wall would mean that only a small proportion of the transducer faceplate would be in contact with the pipe wall). In such a geometry, $P_1(\theta')$ is represented by P_{10}^{actual} when $|\theta'| \le \phi$ and 0 otherwise. When this is substituted into Eq. (12), the coefficient p_{1n} is

$$p_{1n} = \frac{\varepsilon_n}{\pi}\int_{-\phi}^{\phi} P_{10}^{\text{actual}}\cos n\theta' d\theta' = \frac{2P_{10}^{\text{actual}}\varepsilon_n}{\pi}\phi\left(\frac{\sin n\phi}{n\phi}\right). \tag{18}$$

Comparing this with the scenario when a point source is used, as shown in Eq. (17), the coefficient p_{1n} when the actual source is used contains a sinc function. From Fig. 8, the angle ϕ is simply calculated by $\phi = \sin^{-1}(h/d)$ where h is half width of coupling cap.

C. Truncation of infinite sum and pressure distribution

From Eq. (14), the coefficients C, D, E, F, G, and H, can be explicitly calculated. The coefficients E and F are 0. When those are substituted into Eq. (4) in the limit of $k_z \to 0$, the values of τ_{rre}, $\tau_{r\theta e}$, and τ_{rze} are obtained. Among them, τ_{rze} vanishes since $k_z \to 0$ and the coefficients E and F are 0. The pressure in the liquid is calculated by knowing the value of coefficient, A, which is deduced from the continuity of normal displacement in the limit of $k_z \to 0$, that is,

$$\begin{aligned}\left[-k_1 J_{n+1}(k_1 b) + \frac{n}{b}J_n(k_1 b)\right]A &= \left[-k_c J_{n+1}(k_c b) + \frac{n}{b}J_n(k_c b)\right]C \\ &+ \left[-k_c Y_{n+1}(k_c b) + \frac{n}{b}Y_n(k_c b)\right]D \\ &+ \left[\frac{n}{b}J_n(k_s b)\right]G + \left[\frac{n}{b}Y_n(k_s b)\right]H.\end{aligned} \tag{19}$$

Once the value of A is known, the normal stress in the liquid can be also calculated. Since viscosity is disregarded, the shear stresses in the liquid are zero. The total stress is the sum of each term with the index n. Theoretically, the summation may need many terms since so many modes can exist for a given excitation. However, in the numerical regime, the summation should be truncated using criteria that are based upon the size of the actual excitation depicted in Fig. 8. Suppose the acoustic source is generally piston-like and driving a coupling cap whose side facing the outer tube wall is machined to fit to the curvature of the tube. For a given excitation, there exist several circumferential modes. However, the number of existing modes is finite because of the size of the coupling cap. The area of the tube in contact with the coupling cap is characterized by the angle ϕ. Within this area, it may not be possible to excite a mode whose wavelength changes its phase over the dimension of the coupling cap because the source is piston-like. Although the actual coupling cap is not rigid but plastic, the surface of the acoustic source/receiver that is in contact with the coupling caps is a metal (aluminum) and they are tightly mounted on the outer wall of the tube. Because of this, the effect of sudden phase changes of the mode within the size of the plastic coupling cap is minor. Thus, as shown in Fig. 8(b), the minimum wavelength is formed when its half wavelength equals to the width of the coupling cap since it does not changes the sign of its phase as indicated by the dash-dot curve in the picture. Therefore, the condition that the mode can be excited is characterized by the following equation:

$$\frac{\lambda}{2} \ge 2d\phi. \tag{20}$$

The wavelength λ is related to the mode index, n, as $n\lambda = 2\pi d$. When this is substituted into Eq. (20) and the result arranged with respect to the mode index, n, it becomes

$$n \leq \frac{\pi}{2\phi}, \tag{21}$$

where $\phi = \sin^{-1}(h/d)$. Therefore, the maximum mode index that can be excited is the integer satisfying the condition in Eq. (21). For example, when $\phi = \pi/6$, the maximum mode number is 3 and the summation of the series to calculate the stress elements should be truncated at 3. As the angle ϕ increases, the maximum of n decreases. Consequently, when ϕ shrinks to zero to make an ideal point source, the maximum value of possible n becomes infinite, and the stress elements are given as the summation over the infinite series.

D. Distribution of stress

Figure 9 shows the continuous change of the values between the acoustic pressure in the liquid and the normal stress of the pipe for the water-filled PMMA tube system [as shown in Eq. (4a), acoustic pressure in the liquid is the negative of the normal stress]. Different sizes of coupling cap (the outlines of which are drawn either side each pipe) are characterized by the angle ϕ. The bright to dark color scheme represents the positive to negative amplitude of the normal stress. The frequency of the excitation is fixed at 38 kHz. It was assumed that there was no absorption in water or the tube material. Figures 9(a)–9(d) show the magnitudes of the normal stress at given angles of $\phi = \pi/10$, $\phi = \pi/6$, $\phi = \pi/4$, and $\phi = \pi/3$, respectively, which is related to the size of coupling cap that is drawn in outline either side of the pipe. The magnitude of the applied pressure P_{10}^{actual} to the tube wall was set as 1 Pa. The color scheme represents the amplitude of the normal stress in Pascals. The horizontal and vertical position axes are normalized with respect to the outer diameter of the tube. The coupling cap excitation against the wall is introduced and its center is located at the coordinates (1, 0). Two concentric rings represent the inner and the outer boundary of the PMMA tube filled with water. As ϕ increases ($n_{\max}$ decreases), the normal stress distribution becomes axisymmetric. In all cases, the stress distribution is symmetric with respect to both x- and y-axes.

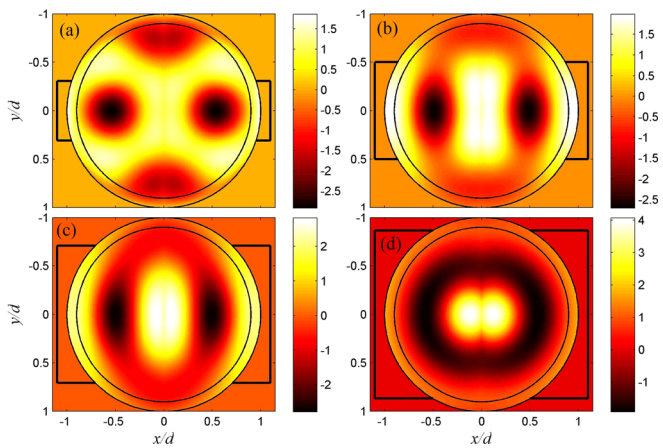

FIG. 9. (Color online) Normal stress in water and PMMA under acoustic excitation of 38 kHz and applied pressure P_{10}^{actual} of 1 Pa. Bright to dark color scheme represents the positive to negative amplitude of the stress in Pa. The coupling cap excitation against the wall is introduced and its center is located at the coordinates of (1, 0) in the picture. The edge of the coupling cap is superimposed on the plot using thick solid black lines to the left and right of the pipe. Different values of ϕ are chosen as (a) $\phi = \pi/10$, (b) $\phi = \pi/6$, (c) $\phi = \pi/4$, (d) $\phi = \pi/3$, respectively, to investigate the effect of ϕ on the stress distribution.

Whilst an infinite number of possible panels could be produced for Fig. 9, four sizes of the coupling caps were selected to show the clear change of the acoustic pressure in the liquid from nonaxisymmetric to axisymmetric distributions as the size of the coupling caps increases (from when the coupling cap fits the size of the smallest transducer faceplate used, to when it covers most of the pipe wall). The four panels show that, for a given frequency (here 38 kHz, the resonance of the smallest transducer used), the size of the coupling cap strongly influences the pressure field in the pipe in the absence of bubbles. The capability to model the bubble-free sound field is important because, when bubbles are added, the local pressure in the liquid at their location is scattered off the bubble and impinges upon the pipe wall (and in turn is partially scattered back onto the bubble[28,29]). The contribution made by bubbles to the pressure field at the pipe wall changes the boundary condition imposed on the liquid-tube interface. Changes in this boundary condition are reflected as changes in the pressure detected by acoustic sensors mounted on the outer surface of the tube, and it is this that is used here to monitor for the presence of bubbles. The principle would work for other scatterers, but the potency of bubble sources would mean they would likely dominate if present. In SNS TTF bubbles are the only inhomogeneities present in the liquid.

Figure 10 shows the shear stress, $\tau_{r\theta}$, distribution for the PMMA tube filled with bubble-free water for different sizes of coupling cap characterized by the angle ϕ. As in Fig. 9, the magnitude of the applied pressure P_{10}^{actual} to the tube wall was set as 1 Pa and bright to dark color scheme represents the positive to negative amplitude of the shear stress in Pascals. The frequency of the excitation is fixed as 38 kHz. Since no viscosity is assumed, the shear stress in water is 0. The shear stress, τ_{rz} is automatically 0 in purely cross-sectional problems. Looking at the distribution of the shear stress, as ϕ increases ($n_{\max}$ decreases), the number of nodes distributed along the tube decreases since the mode behaves more axisymmetrically, which decreases the level of the shear stress. In the extreme case that $n_{\max}$ is less than 1 (the axisymmetric case), the shear stress vanishes even inside the tube walls since $\tau_{r\theta}$ is automatically 0 when $n = 0$. This explains the low values seen in Fig. 10(d) compared to Fig. 10(a). The absorption of PMMA takes a negligible role in the circumferentially formed stress due to the very short dimension of the pipe cross section compared to the material absorption. The eventual usage of the forced excitation is intended for the steel pipelines where the material absorption is much smaller than that of PMMA tube. For this reason the absorption of PMMA was neglected in these simulations since, when transferred to the actual ORNL SNS TTF case, the absorption parameter would be set to 0. Hence the simulations here neglect the effect of absorption in the calculation of stress.

Whereas Fig. 9 showed finite acoustic pressures (the negative of the normal stress) in the liquid, in Fig. 10 there is

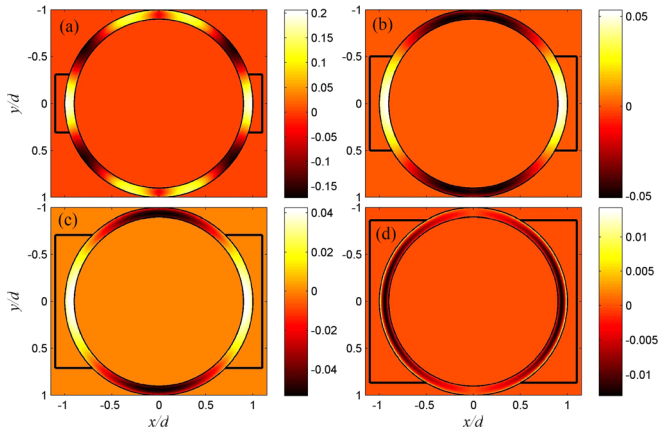

FIG. 10. (Color online) Shear stress $\tau_{r\theta}$ in water and PMMA under acoustic excitation of 38 kHz and applied pressure P_{10}^{actual} of 1 Pa. Bright to dark color scheme represents the positive to negative amplitude of the stress in Pa. The coupling cap excitation against the wall is introduced and its center is located at the coordinates of (1, 0) in the picture. The edge of the coupling cap is superimposed on the plot using thick solid black lines to the left and right of the pipe. Different values of ϕ are chosen as (a) $\phi = \pi/10$, (b) $\phi = \pi/6$, (c) $\phi = \pi/4$, (d) $\phi = \pi/3$, respectively, to investigate the effect of ϕ on the stress distribution. Since no viscosity was assumed, the shear stress in water is zero.

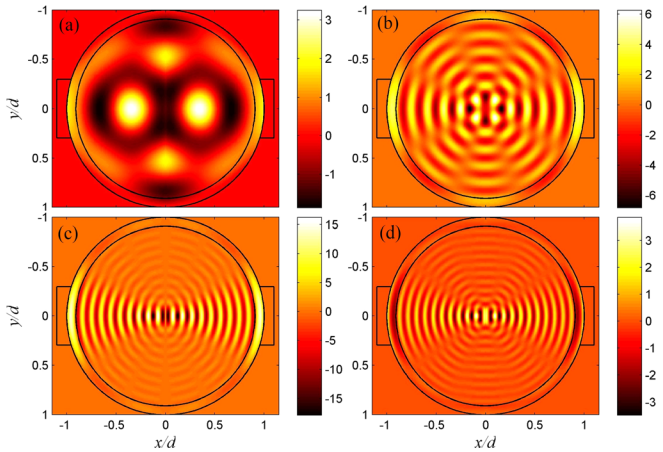

FIG. 11. (Color online) Normal stress in water and PMMA tube with the same dimension of the ORNL pipeline under different acoustic excitation of (a) 38 kHz, (b) 128 kHz, (c) 220 kHz, and (d) 245 kHz, respectively. Bright to dark color scheme represents the positive to negative amplitude of the stress in Pa. The coupling cap excitation against the wall is introduced with the applied pressure P_{10}^{actual} of 1 Pa, and its center is located at the coordinates of (1, 0) in the picture. The edge of the coupling cap is superimposed on the plot using thick solid black lines to the left and right of the pipe. Angle ϕ was fixed throughout the figure by $\phi = \sin^{-1}(h/d)$ where $d = 7.065$ cm and $h = 2.1$ cm.

of course no stress (shear stress) in the liquid (because of course it is assumed to be inviscid). As a result, bubbles in an inviscid liquid cannot affect the shear stress in the pipe wall, and consequently the detector will be based on the normal stresses in the wall.

The contract with ORNL required that the device be taken to ORNL, fitted to SNS TTF, and measure bubbles. However the cost and hazard of building a 1:1 scale test rig in Southampton using flowing mercury in steel pipelines was prohibitive, and so modeling was undertaken to test whether a suitable 1:1 scale model could be built using flowing water in PMMA pipelines. To do this the acoustic pressure in the liquid and the normal stress in the pipe material were plotted in Fig. 11 (for bubble-free water in PMMA pipes) and in Fig. 12 (for bubble-free mercury in steel pipes) for the four frequencies at which the sensors operated [(a) 38 kHz, (b) 128 kHz, (c) 220 kHz, and (d) 245 kHz], for the size of coupling cap that was actually used. The objective was to determine the differences in the stress generated in the two cases. This was to allow assessment of the modifications that would be needed to be made to a sensor that had been tested and calibrated on a water-filled PMMA pipe, when those sensors were deployed on ORNL's mercury-filled steel pipes. The dimensions of the tube systems in Figs. 11 and 12 are the same as those of the steel/mercury tube in ORNL, that is, 6.4097 cm inner radius and 0.6553 cm thickness (the dimensions used to build the 1:1 PMMA/water model at Southampton).

Figure 11 shows the continuous change of the values between the acoustic pressure in the liquid and the normal stress of the pipe for the PMMA tube filled with water at the four frequencies. Four frequencies were selected to show the strong concentration of the acoustic pressure in the liquid along the direction that the sensors are facing with each other as the excitation frequency increases. The bright to dark color scheme represents the positive to negative amplitude of the normal stress in Pascals. The material parameters are the same as those in Figs. 9 and 10. The magnitude of the applied pressure P_{10}^{actual} to the tube wall was set at 1 Pa. The angle ϕ was fixed so that h is 2.1 cm, which means that $n_{\max}$ is fixed and, with this system dimension, $n_{\max}$ is 5. In order to show the features clearly, the color bar in each panel extends from the minimum to the maximum amplitude of each stress distribution. As the frequency increases, more nodes are formed inside the tube along the radial direction, since higher frequencies are associated with smaller wavelengths.

Figure 12 shows the continuous change of the values between the acoustic pressure in the liquid and the normal stress of the pipe for the steel tube filled with liquid mercury

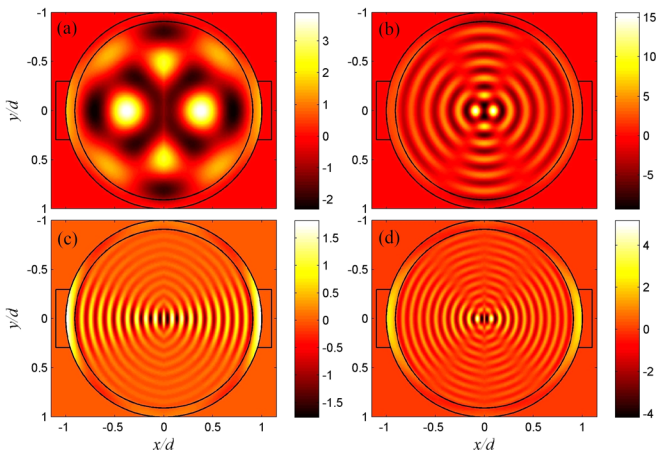

FIG. 12. (Color online) Normal stress in mercury and steel under different acoustic excitation of (a) 38 kHz, (b) 128 kHz, (c) 220 kHz, and (d) 245 kHz, respectively. Bright to dark color scheme represents the positive to negative amplitude of the stress in Pa. The coupling cap excitation against the wall is introduced with the applied pressure P_{10}^{actual} of 1 Pa, and its center is located at the coordinates of (1, 0) in the picture. The edge of the coupling cap is superimposed on the plot using thick solid black lines to the left and right of the pipe. Angle ϕ was fixed throughout the figure by $\phi = \sin^{-1}(h/d)$ where $d = 7.065$ cm and $h = 2.1$ cm.

for the same four excitation frequencies as Fig. 11. The bright to dark color scheme represents the positive to negative amplitude of the normal stress. The material parameters used in the calculation are as follows: The densities of steel and mercury are $7900\,\mathrm{kg\,m^{-3}}$ and $13\,500\,\mathrm{kg\,m^{-3}}$, respectively. The shear and longitudinal wave speeds in steel are $5675\,\mathrm{m\,s^{-1}}$ and $3140\,\mathrm{m\,s^{-1}}$, respectively, which makes the Poisson's ratio of the material take a value of 0.2792. The intrinsic sound velocity in mercury is assumed to be $1451\,\mathrm{m\,s^{-1}}$. Comparing Fig. 12 with Fig. 11, the patterns at each frequency are very similar with each other. This similarity is used to justify building a 1:1 scale model of the mercury-filled steel pipework of TTF SNS out of water-filled PMMA pipes of the same dimension, in order to provide a safe (mercury-free) test bed for the sensor before it was transported out to ORNL, Tennessee.

V. CONCLUSION

A theory to describe the dispersion curves for the axially propagating nonaxisymmetric modes in liquid-filled tube was developed and compared with measurements. This theory was applied to the dispersion curve for the circumferential modes. The resonance frequency of each circumferential mode was calculated and compared with the Finite Element results. The stress distributions in the liquid and the tube were theoretically calculated by the summation of the circumferential modes when acted upon by an external acoustic source which drives the outer surface of the tube. The code was used to justify the building of an inexpensive, safe 1:1 scale model of ORNL's SNS TTF consisting of water in PMMA pipes, in order to provide a test bed for the sensors, prior to their being transported to Tennessee for use.

ACKNOWLEDGMENT

This work is supported by the Oak Ridge National Laboratory (ORNL), TN (ORNL is managed by UT-Battelle, LLC, under contract DE-AC05-00OR22725 for the U.S. Department of Energy) and by the UK Science and Technology Research Council Rutherford Appleton Laboratory. The authors are very grateful to Bernie Riemer and Mark Wendel of ORNL, and Chris Densham, Ottone Caretta, and Tristan Davenne of RAL, for advice and discussions. We are particularly grateful to Bernie Riemer, Mark Wendel, Robert (Bob) L. Sangrey for useful discussion and access to the TTF Facility.

[1]Lord Rayleigh, "On waves propagating along the plane surface of an elastic solid," Proc. Lond. Math. Soc. **17**, 4–11 (1885).
[2]P. M. Morse, "Some aspects of the theory of room acoustics," J. Acoust. Soc. Am. **11**, 56–66 (1939).
[3]P. M. Morse, "The transmission of sound inside pipes," J. Acoust. Soc. Am. **11**, 205–210 (1939).
[4]W. J. Jacobi, "Propagation of sound waves along liquid cylinders," J. Acoust. Soc. Am. **21**, 120–127 (1949).
[5]T. C. Lin and G. W. Morgan, "Wave propagation through fluid contained in a cylindrical, elastic shell," J. Acoust. Soc. Am. **28**, 1165–1176 (1956).
[6]J. C. F. Chow and J. T. Apter, "Wave propagation in a viscous incompressible fluid contained in flexible viscoelastic tubes," J. Acoust. Soc. Am. **44**, 437–443 (1968).
[7]V. A. Del Grosso, "Analysis of multimode acoustic propagation in liquid cylinders with realistic boundary conditions—Application to sound speed and absorption measurements," Acustica **24**, 299–311 (1971).
[8]L. D. Lafleur and F. D. Shields, "Low-frequency propagation modes in a liquid-filled elastic tube waveguide," J. Acoust. Soc. Am. **97**, 1435–1445 (1995).
[9]B. K. Sinha, T. J. Plona, S. Kostek, and S. K. Chang, "Axisymmetric wave propagation in fluid-loaded cylindrical shell. I. Theory," J. Acoust. Soc. Am. **92**, 1132–1143 (1992).
[10]T. J. Plona, B. K. Sinha, S. Kostek, and S. K. Chang, "Axisymmetric wave propagation in fluid-loaded cylindrical shell. II. Theory versus experiment," J. Acoust. Soc. Am. **92**, 1144–1155 (1992).
[11]K. Baik, J. Jiang, and T. G. Leighton, "Acoustic attenuation, phase and group velocities in liquid-filled pipes: Theory, experiment, and examples of water and mercury," J. Acoust. Soc. Am. **128**, 2610–2624 (2010).
[12]J. Jiang, K. Baik, and T. G. Leighton, "Acoustic attenuation, phase and group velocities in liquid-filled pipes II: Simulation for spallation neutron sources and planetary exploration," J. Acoust. Soc. Am. **130**, 695–706 (2011).
[13]D. C. Gazis, "Three-dimensional investigation of the propagation of waves in hollow circular cylinders. I. Analytical foundation," J. Acoust. Soc. Am. **31**, 568–573 (1959).
[14]C. R. Fuller and F. J. Fahy, "Characteristics of wave propagation and energy distributions in cylindrical elastic shells filled with fluid," J. Sound Vib. **81**, 501–518 (1982).
[15]J. E. Greenspon and E. G. Singer, "Propagation in fluids inside thick viscoelastic cylinders," J. Acoust. Soc. Am. **97**, 3502–3509 (1995).
[16]B. N. Pavlakovic, M. J. S. Lowe, D. N. Alleyne, and P. Cawley, "DISPERSE: A general purpose program for creating dispersion curves," in *Review of the Progress in Quantitative Nondestructive Evaluation*, edited by D. O. Thompson and D. E. Chimenti (Plenum Press, New York, 1997), Vol. 16A, pp. 185–192.
[17]B. N. Pavlakovic and M. J. S. Lowe, "A general purpose approach to calculating the longitudinal and flexural modes of multi-layered, embedded, transversely isotropic cylinders," in *Review of the Progress in Quantitative Nondestructive Evaluation*, edited by D. O. Thompson and D. E. Chimenti (Plenum Press, New York, 1999), Vol. 18A, pp. 239–246.
[18]X. L. Bao, P. K. Raju, and H. Überall, "Circumferential waves on an immersed, fluid-filled elastic cylindrical shell," J. Acoust. Soc. Am. **97**, 2704–2709 (1999).
[19]X. L. Bao, H. Überall, P. K. Raju, A. C. Ahyi, I. K. Bjørnø, and L. Bjørnø, "Waves on fluid-loaded shells and their resonance frequency spectrum," J. Sound Vib. **287**, 383–394 (2005).
[20]G. T. Yim and T. G. Leighton, "Real-time on-line ultrasonic monitoring for bubble in ceramic 'slip' in pottery pipelines," Ultrasonics **50**, 60–67 (2010).
[21]T. G. Leighton, K. Baik, and J. Jiang, "The use of acoustic inversion to estimate the bubble size distribution in pipelines," Proc. R. Soc. A. **468**, 2461–2484 (2012).
[22]T. G. Leighton, J. Jiang, and K. Baik, "A TV demonstration of sound absorption connecting the space shuttle to submarines," Acoust. Bull. **36**, 35–40 (2011).
[23]M. Futakawa, H. Kogawa, S. Hasegawa, Y. Ikeda, B. Riemer, M. Wendel, J. Haines, G. Bauer, T. Naoe, K. Okita, A. Fijiwara, Y. Matsumoto, and N. Tanaka, "Cavitation damage prediction for spallation target vessels by assessment of acoustic vibration," J. Nucl. Mat. **77**, 182–188 (2008).
[24]N. Manzi, P. V. Chitnis, R. G. Holt, R. A. Roy, R. O. Cleveland, B. Riemer, and M. Wendel, "Detecting cavitation in mercury exposed to a high-energy pulsed proton beam," J. Acoust. Soc. Am. **127**, 2231–2239 (2010).
[25]M. Abramowitz and I. A. Stegun, *Handbook of Mathematical Functions* (Dover, New York, 1964), pp. 361.
[26]T. G. Leighton, J. Jiang, and K. Baik, "Demonstration comparing sound wave attenuation inside pipes containing bubbly water and water droplet fog," J. Acoust. Soc. Am. **131**, 2413–2421 (2012).
[27]B. Hartmann and J. Jarzynski, "Ultrasonic hysteresis absorption in polymers." J. Appl. Phys. **43**, 4304–4312 (1972).
[28]T. G. Leighton, D. G. Ramble, A. D. Phelps, C. L. Morfey, and P. P. Harris, "Acoustic detection of gas bubbles in a pipe," Acust. Acta Acust. **84**, 801–814 (1998).
[29]T. G. Leighton, P. R. White, C. L. Morfey, J. W. L. Clarke, G. J. Heald, H. A. Dumbrell, and K. R. Holland "The effect of reverberation on the damping of bubbles," J. Acoust. Soc. Am., **112**, 1366–1376 (2002).